CHEMISTRY OF MATERIALS

ARTICLE

pubs.acs.org/cm

Meso-channel Development in Graphitic Carbon Nanofibers with Various Structures

Donghui Long,*,† Wei Li,‡ Jin Miyawaki,‡ Wenming Qiao,† Licheng Ling,† Isao Mochida,‡ and Seong-Ho Yoon*,‡

†State Key Laboratory of Chemical Engineering, East China University of Science and Technology, Shanghai 200237, China

‡Institute for Materials Chemistry and Engineering, Kyushu University, Kasuga, Fukuoka 816-8580, Japan

Supporting Information

ABSTRACT: A general method based on oxidation and heat expansion was developed to introduce mesoporous channels into the catalytically grown carbon nanofibers (CNFs) with platelet, herringbone, and tubular structures. Strong oxidation of CNFs caused large amounts of oxygen functionalities to be intercalated in the *c*-plane of the graphene layers, increasing the interlayer spacing. These intercalated components vaporized rapidly during the heat treatment, forcing apart adjacent graphene sheets and, thus, forming mesoporous channels. The obtained mesoporous CNFs maintained the fibrous form and the graphene layer alignment of their parent CNFs, but they developed aligned mesoporous channels. These channels reflected the intrinsic structure of the CNFs, which would be further adjusted by changing the oxidation degree of the CNFs or the initial crystalline structure of the CNFs. The development of mesoporous channels increased remarkably the external surface area of CNFs. It has further been demonstrated that these mesoporous CNF supported Pt nanoparticles exhibited fairly high electrocalaytic activity for methanol oxidation. As a result of their large external surface area and good crystalline structure, these mesoporous CNFs should be excellent supports for the electrodes of direct methanol fuel cells.

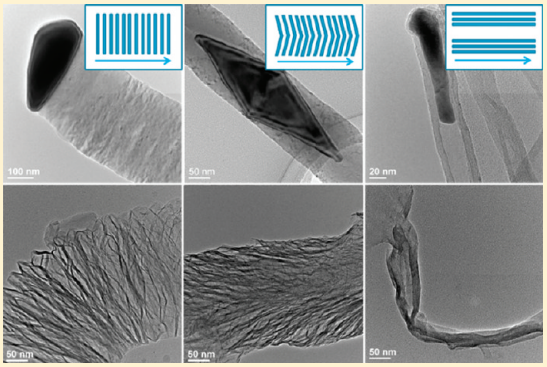

KEYWORDS: carbon nanotube, carbon nanofibers, mesopore, fuel cell

INTRODUCTION

Catalytically grown carbon nanotubes (CNTs) and carbon nanofibers (CNFs) are recognized as unique nanosized fibrous forms of graphitic materials produced by the decomposition of selected hydrocarbons over hot metal particles.[1−4] These nanomaterials possess a unique combination of physical and chemical properties due to highly ordered nanoscale graphene layers.[5,6] Three main types of CNFs exist and are categorized on the basis of the alignment of the graphene layers: platelet CNFs (PCNFs, aligned perpendicular to the fiber axis), tubular CNFs (TCNFs, aligned parallel to the axis, also known as CNTs), and herringbone CNFs (HCNFs, tilted to the axis).[7] These diverse structures make CNFs attractive for potential applications in electrochemical energy storage,[8,9] hydrogen storage,[10,11] composites,[12] and catalysis.[13,14]

A drawback of CNFs is their nonporous surface structure, which limits their applicability in catalysis and adsorption where porosity is crucial.[15] Inserting pores into CNFs could increase their surface area and enhance the areal density of surface defects, which should greatly improve their properties and broaden their applications. There are some reports on introducing porosity into CNTs or CNFs, based on direct gasification of carbon[16,17] or chemical activation by KOH.[18−20] These methods are mainly designed to enhance the surface oxygen content or to develop micropores on the external surface of CNFs. Currently, however, no efficient method exists to introduce mesopores into CNFs with highly graphitic crystallinity and various graphene layer alignments.

Here, we developed a simple method to introduce mesoporous channels into catalytically grown CNFs with various graphene layer alignments. CNFs with platelet, herringbone, and tubular structures were used as starting materials and oxidized by $KMnO_4$ in concentrated sulfuric acid (H_2SO_4). Oxidized CNFs had graphite oxide structures[21] and can be readily expanded to form mesoporous channels into CNFs by heat treatment. The resulting CNFs inherited the fibrous form and the graphene layer alignment of their parent CNFs, but the mesopores were inserted against the *c*-axis of the graphitic layers. This method for introducing mesopores in CNFs will provide potential materials for applications in energy storage, adsorption, separation, and catalysis.

EXPERIMENTAL SECTION

Preparation of CNFs. Three types of CNFs, platelet, herringbone, and tubular structures, were used in this study.[22,23] Platelet CNFs (PCNFs) were synthesized from carbon monoxide and hydrogen

Received: March 30, 2011
Revised: July 31, 2011
Published: August 22, 2011

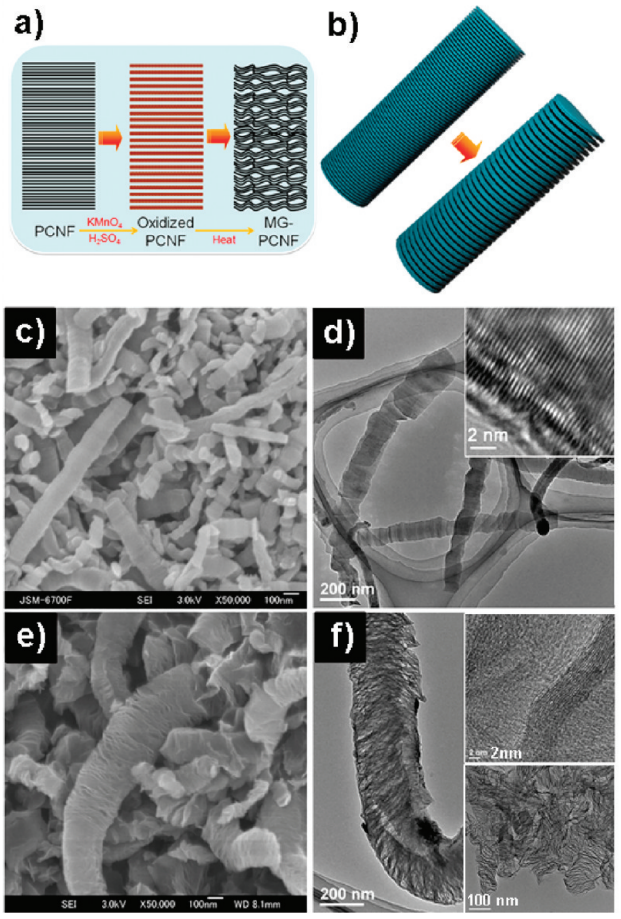

Figure 1. (a) Schematic of preparation of MG-PCNFs from as-prepared PCNFs. (b) 3D model of PCNFs and MG-PCNFs. (c) SEM and (d) TEM images of as-prepared PCNFs. (e) SEM and (f) TEM images of MG-PCNFs.

(160/40, v/v, mL min^{-1}) over an Fe catalyst at 600 °C. Herringbone CNFs (HCNFs) were synthesized from carbon monoxide and hydrogen (160/40, v/v, mL min^{-1}) over an Fe−Ni−Co−MgO catalyst (7/0.5/0.5/2, weight ratio) at 560 °C. Tubular CNFs (TCNFs) were synthesized from carbon monoxide and hydrogen (40/160, v/v, mL min^{-1}) over an Fe−Ni catalyst (6/4, weight ratio) at 640 °C. Some CNFs were further heat-treated at 2800 °C for 10 min to obtain graphitized CNFs.

Preparation of MG-CNFs. CNFs were oxidized according to the Hummer method.[24] Typically, 1 g of PCNTs was suspended in 100 mL of concentrated H_2SO_4 for 12 h, and then, 3 g of $KMnO_4$ was added slowly. The reaction mixture was stirred at 0 °C for 30 min and heated to 40 °C for 1 h. For herringbone and tubular CNFs, the latter temperature was raised to 70 °C. The reaction was quenched by pouring the mixture over ice containing 30 mL of hydrogen peroxide (H_2O_2). The solution was separated using a centrifuge at 4800 rpm. The remaining slurry was washed with a 1 M HCl solution and distilled water until the pH was ~4. The slurries were then dried in an oven at 80 °C for 24 h. MG-CNFs were obtained by rapid heat treatment in a N_2 atmosphere at 300 °C with the heating rate 30 °C min^{-1} and carbonization at 900 °C for 3 h with the heating rate 5 °C min^{-1}.

Preparation and Electrochemical Testing of Pt/MG-CNFs. MG-CNFs supported Pt nanoparticles (Pt/MG-CNFs) were prepared by a modified ployol reduction method.[25] To a flask in an ice bath were added 100 mg of MG-CNFs, 20 wt % $H_2PtCl_6 \cdot 4H_2O$, 100 mL of H_2O, and 100 mL of ethylene glycol (EG). This solution was mixed under ultrasonic iced water bath for 1 h. After this treatment, the solution was heated to 60 °C with magnetic stirring for 24 h and separated by filtration. The powders were washed several times with deionized water and dried in a vacuum oven at 80 °C overnight.

Cyclic voltammetry (CV) measurements were conducted using a three electrode cell at 25 °C. Pt gauze and Ag/AgCl (in saturated KCl) were used as the counterelectrode and reference electrode, respectively. The commercial carbon-supported Pt (40 wt %) catalyst was obtained from Suntel Co. The catalyst ink consisting of catalyst, Nafion ionomer (in water), and 2-propanol was dropped onto the gold working electrode and dried at 70 °C in a vacuum oven. CV was used to study the electrocatalytic active areas (ECSAs) and electrocatalytic activities of the Pt/MG-CNFs. CV measurements were acquired in a 0.5 M H_2SO_4 solution or a 1.0 M CH_3OH/0.5 M H_2SO_4 solution using a three-electrode system. The membrane electrode assembly for DMFC single cell tests was fabricated and tested in Suntel Co. The cell temperature was fixed at 70 °C.

Characterization. X-ray diffraction (XRD) was performed using a Rigaku X-ray diffractometer with a Cu Kα target. Porosity was measured with nitrogen adsorption−desorption isotherms at 77 K, using a surface area analyzer (Sorptomatic 1990, Qunata Instruments). The Brunauer−Emmett−Teller (BET) method was utilized to calculate the specific surface areas. The total pore volume was estimated from the adsorbed amount at a relative pressure of $P/P_0 = 0.985$. The average pore size was derived from the adsorption branch by using the Barrett−Joyner−Halenda (BJH) model. High-resolution solid-state ^{13}C nuclear magnetic resonance (NMR) experiments were carried out on a JEOL ECA400 spectrometer operated at 100.53 MHz using the single-pulse decoupling method. The spinning speed of the MAS NMR is 75 with a 1.2 mm rotor. The structure was observed under a field-emission scanning electron microscope (FE-SEM; JEOL-6300F) and a high-resolution transmission electron microscope (TEM; JEM-2010F, 200 kV). Elemental compositions were obtained from CHN elemental analysis (Yanako MT2 CHN Corder). X-ray photoelectron spectroscopy (XPS) spectra were acquired using a JPS-9000MC (JEOL) instrument equipped with an Mg Kα X-ray source.

RESULTS AND DISCUSSION

Preparation of Platelet MG-CNFs. The overall synthetic procedure for preparation of platelet MG-CNFs is represented in Figure 1a. Platelet CNFs were characterized by graphene layers aligned perpendicular against the fiber axis. The as-prepared PCNFs had diameters of 80−350 nm with a polygonal cross section, based on SEM observation (Figure 1c). TEM images (Figure 1 d) showed that the graphene layers were stacked in a direction perpendicular to the fiber axis and separated by a distance of ~0.335 nm. The PCNFs were oxidized in concentrated H_2SO_4 with 300 wt % $KMnO_4$ according to Hummer's method.[22] The oxidized PCNFs were expanded by heat treatment to form mesoporous graphitic PCNFs (MG-PCNFs). SEM and TEM images in Figure 1e and f clearly revealed that MG-PCNFs adopted the original fibrous form but developed mesoporous channels perpendicular to the fiber axis. These mesoporous channels originated from the space between twisted graphene plates (as illustrated in Figure 1a and b). Lattice image observation (Figure 1f, inset) indicated that the in-plane size of graphene plates was ~4 nm, equivalent to ~10 graphene layers. The *c*-axis interlayer distance was in the range 0.35−0.41 nm, slightly larger than that of the parent PCNFs.

The structural evolution from the parent PCNFs to the oxidized PCNFs and, finally, to the MG-PCNFs was monitored by XRD, XPS, solid-state ^{13}C (NMR), and N_2 adsorption (Figure 2). The parent structure of the PCNFs was nearly nonporous with a BET

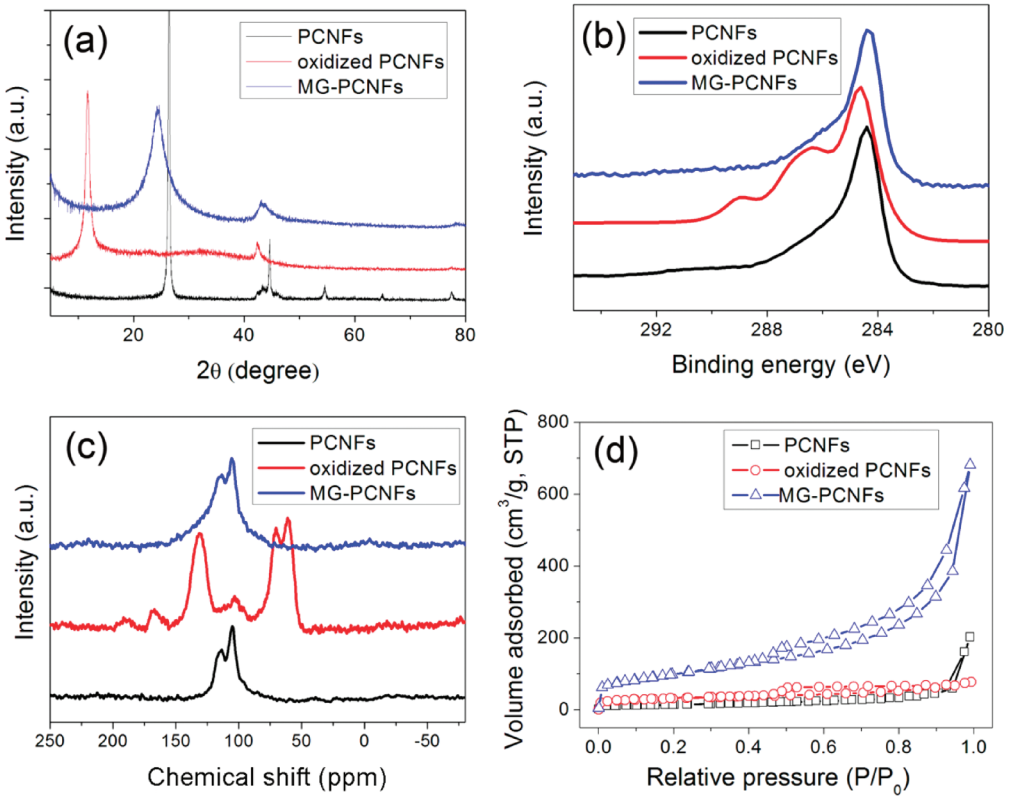

Figure 2. Structural evolution from PCNFs to mesoporous graphitic PCNFs (MG-PCNFs) monitored by XRD (a), XPS (b), solid ^{13}C NMR (c), and N_2 adsorption (d).

surface area of 56 $m^2\ g^{-1}$. XRD patterns (Figure 2a) revealed that the PCNFs exhibited a high degree of graphitization, close to that of graphite, with the interlayer distance $d_{002} \sim 0.336$ nm. After oxidation, the XRD pattern showed a new peak at ~10° (d value 0.71 nm) corresponding to a graphite oxide-like structure.[21] XPS spectra revealed that the oxidized PCNFs contained various amounts of oxygen functionalities and that the most dominant were hydroxyls, —C—OH, carbonyls, —C═O, and carboxyls, —COOH (Supporting Information, Figure S1). The solid ^{13}C NMR spectrum of the pristine PCNFs showed two peaks at 105 and 120 ppm, which should be ascribed to the conjugated double groups and the aromatic double groups, respectively. After the oxidation, the NMR spectrum exhibited five peaks centered at 60, 70, 105, 130, and 165 ppm, corresponding to C—OH, C—O—C epoxide, conjugated double groups, aromatic entities, and carboxylic groups, respectively (Figure 2c), which is consistent with a graphite oxide structure.[26−28] These results suggested that the oxidation of PCNFs was similar to that of graphite, in which oxidation by permanganate in acid introduced epoxy and hydroxyl groups in the graphene layers and introduced carboxylic groups on the edges of the layers. Oxidation caused large amounts of oxygen functionalities to be intercalated in the c-plane of the graphene layers, increasing the interlayer spacing from 0.336 to 0.71 nm and forming the graphite oxide-like structure in the PCNFs.

Rapid heating of the oxidized PCNFs to 300 °C caused violent formation of volatile gaseous species from the intercalated components, forcing apart adjacent graphene sheets. This thermal expansion step is critical and responsible for the formation of MG-PCNFs; it was evidenced by a visible, dramatic volume expansion of PCNFs by ~50−100 times after the heating. Further 900 °C treatment can further reverse oxidation by thermally desorbing covalently attached species and repair defects. XRD, XPS, and NMR results (shown in Figure 2) have confirmed the remarkable recovery of the graphitic structure in the obtained MG-PCNFs. The MG-PCNFs had d_{002} = 0.36 nm and Lc = 3.8 nm with ca. 10 layers of stacking, in agreement with the TEM observation. The MG-PCNFs exhibited slit-shaped mesopores, as illustrated by a typical type-IV isotherm with an H3 hysteresis loop. The BET specific surface area of MG-PCNFs was 355 $m^2\ g^{-1}$, six times greater than that of the parent PCNFs. The total pore volume was 1.2 $cm^3\ g^{-1}$, and the mean pore size was 3.17 nm. No micropores were detected, suggesting the increase of surface area was contributed only by the expanded external surface of PCNFs.

The porosity of MG-PCNFs can be adjusted by varying the oxidation degree of PCNFs. The oxidation degree of PCNFs was controlled by the mass ratio of $KMnO_4$/PCNFs (R), which was confirmed by elemental analysis, XRD (Figure 3a), solid ^{13}C NMR (Figure 3b), and XPS (Supporting Information, Figure S1) techniques. With an increase of the R value from 1 to 5, the O/C atomic ratio changed from the lowest oxidation state of 0.09 to an intermediate oxidation state of 0.51 (R = 3) and then to a high oxidation state of 0.72 (R = 5). XRD and NMR results revealed that the graphite oxide-like structure could not be obtained at R = 1. Increasing the R value caused a high oxidation degree and the formation of a graphite oxide structure. The d_{002} peak of XRD pattern shifted to a lower diffraction angle with further increasing of the R value, revealing the increase of the layer distance. However, there were no obvious differences existing in the solid ^{13}C NMR spectra of highly oxidized PCNFs.

dx.doi.org/10.1021/cm200892c |*Chem. Mater.* 2011, 23, 4141–4148

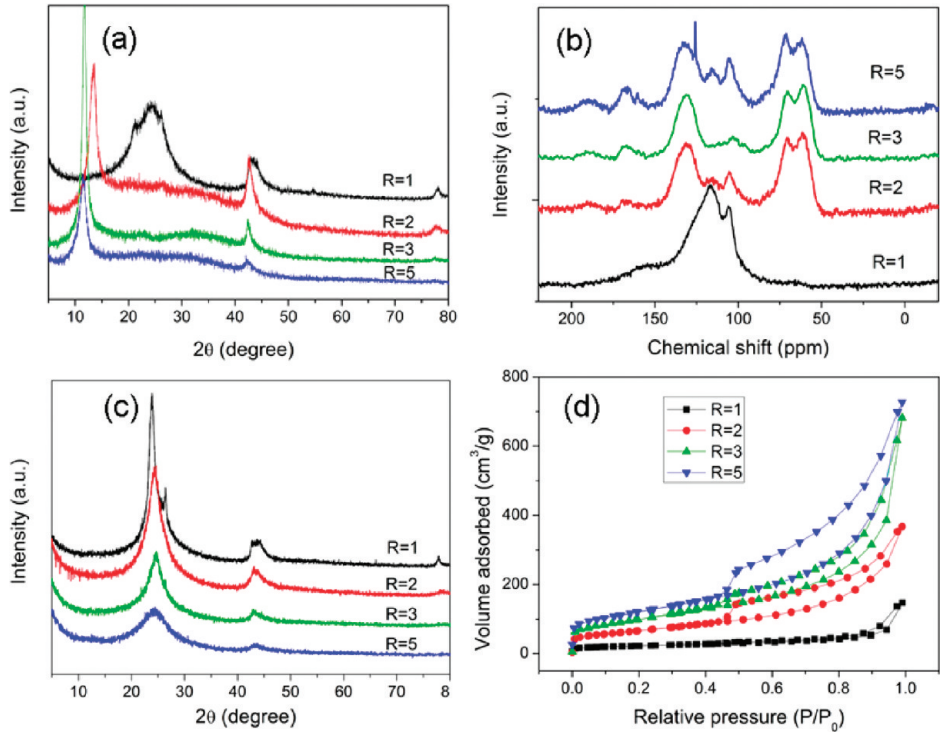

Figure 3. Structural control of mesoporous graphitic PCNFs (MG-PCNFs): (a) XRD patterns of oxidized PCNFs with different KMnO4/PCNF (R) values, (b) solid ^{13}C NMR spectra of oxidized PCNFs with different R values, (c) XRD patterns of MG-PCNFs with different R values, and (d) N_2 adsorption−desorption isotherms of MG-PCNFs with different R values.

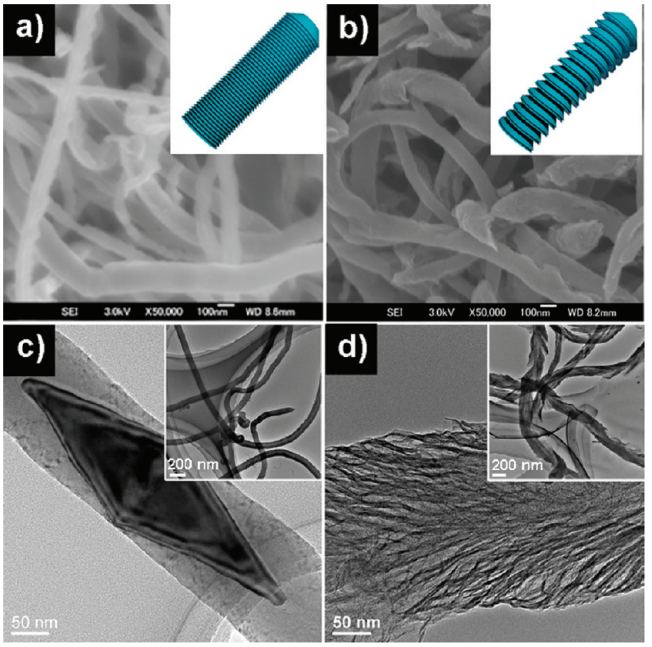

Figure 4. SEM and TEM images of as-prepared herringbone CNFs (a and c) and mesoporous herringbone MG-CNFs (b and d).

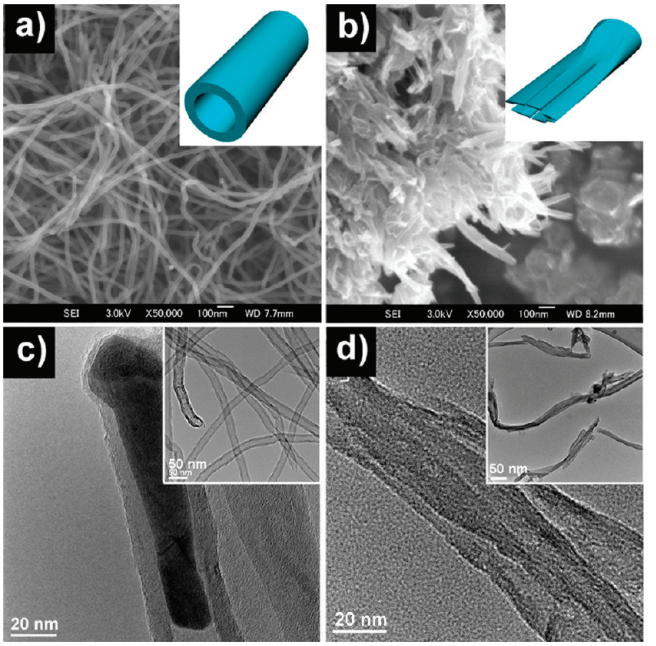

Figure 5. SEM and TEM images of as-prepared tubular CNFs (a and c) and mesoporous tubular MG-CNFs (b and d).

After the two-step heat treatment, the graphite oxide-like structure disappeared and the sp^2 structure of carbon recovered greatly. Figure 3c showed the XRD patterns of the MG-PCNFs with different oxidation degrees. The peak at ~25° broadened, and its intensity decreased gradually with the increase of the R value. Mesopores were introduced into MG-PCNFs, while the R value was 2, as confirmed by the typical type-IV isotherm in Figure 3d. The BET surface areas of the MG-PCNFs with R values of 1, 2, 3, and 5 were 69, 220, 355, and 429 $m^2\ g^{-1}$, respectively. The total pore volume increased from 0.2 to 1.35 $cm^3\ g^{-1}$.

dx.doi.org/10.1021/cm200892c |*Chem. Mater.* 2011, 23, 4141–4148

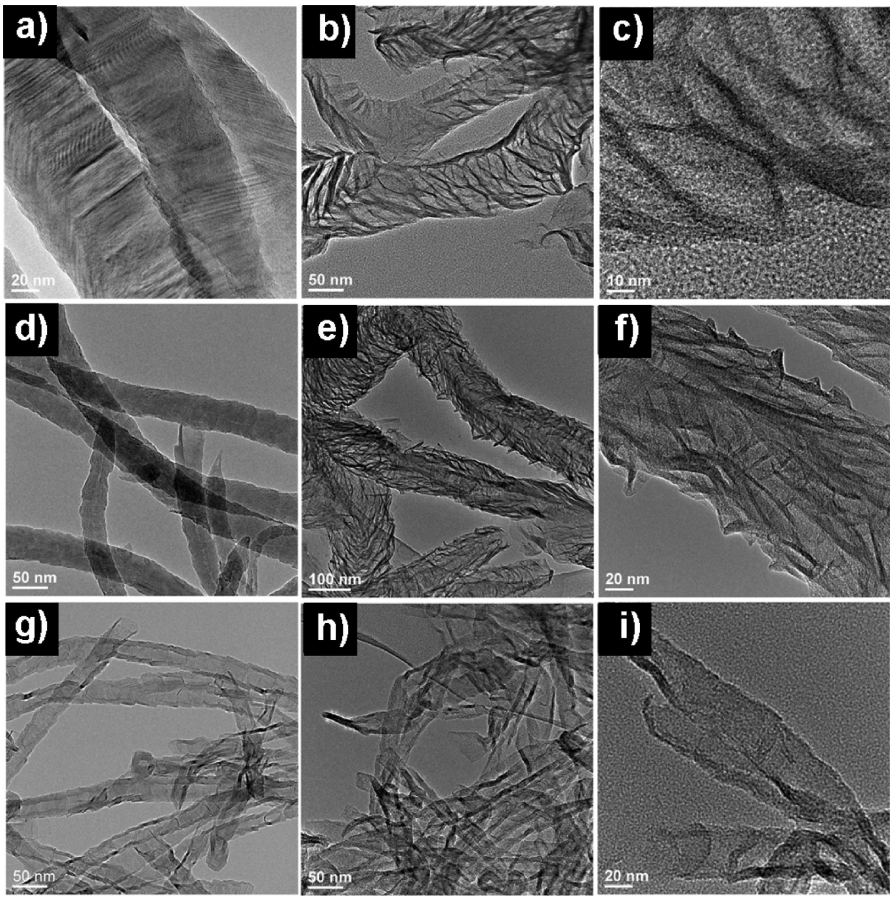

Figure 6. TEM images of graphitized PCNFs (a), mesoporous graphitic GPCNFs (b, c), graphitized HCNFs (d), mesoporous graphitic GHCNFs (e, f), graphitized TCNFs (g), and mesoporous graphitic GTCNFs (h, i).

Their mesopore sizes were 3.27, 3.17, and 3.54 nm for R = 2, 3, and 5, respectively. TEM observation showed that the MG-PCNFs retained their fibrous form until R = 5 (Supporting Information, Figure S2). In these cases, severe oxidation would break the PCNFs into small pieces, and upon thermal expansion, these small pieces aggregated and lost their fibrous form.

Preparation of Herringbone and Tubular MG-CNFs. Similarly, the mesoporous channels of herringbone CNFs were inserted parallel to the graphene layers, which were angled to the fiber axis. The HCNFs used here had an average diameter ~100 nm (Figure 4a and c). The TEM image revealed that the graphene layers aligned with a tilt angle of 30° against the fiber, providing a smaller amount of free edges on the external surface compared to those of the PCNFs. Thus, the oxidation of HCNFs to graphite oxide-like structures was relatively difficult. We used a higher reaction temperature (70 °C) to oxidize the HCNFs. After oxidation, HCNFs exhibited both a graphitic structure and a graphite oxide-like structure (Supporting Information, Figure S3). The heat treatment caused the oxidized HCNFs to expand into MG-HCNFs with radially oriented pores (Figure 4b and d), reflecting the herringbone alignment of the HCNFs. The MG-HCNFs had median BET surface area = 227 $m^2\ g^{-1}$ and total pore volume = 0.6 $cm^3\ g^{-1}$. Their average mesopore size was 3.47 nm, similar to that of the MG-PCNFs (Supporting Information, Figure S4).

Tubular CNFs, popular as carbon nanotubes, are concentric structures with curved graphene planes parallel to the fiber axis. Thus, the TCNFs were relatively inert to oxidation. Under severe oxidation conditions, the TCNFs with an average diameter of 25 nm (Figure 5a and c) were successfully oxidized to graphite oxide structures (Supporting Information, Figure S3). After heat treatment, the tubes were longitudinally unzipped into several graphene nanoribbons, as shown in Figure 5b and d. These nanoribbons were not completely isolated because their tips were still linked together, forming a besomlike structure. The spaces between these nanoribbons constituted mesoporous channels parallel to the fiber axis. The obtained MG-TCNFs had a lowest BET surface area = 168 $m^2\ g^{-1}$ and total pore volume = 0.35 $cm^3\ g^{-1}$. Their average mesopore size was 3.14 nm.

Preparation of Mesoporous Graphitized CNFs. The initial degree of graphitization for the CNFs was important in determining the mesoporous structure. The amorphous carbon, or less-graphitic carbon, was extremely labile, causing excessive oxidation and loss of the fibrous form. For example, the platelet CNFs prepared at 500 °C had a low degree of graphitization. Thus, oxidizing them into bulk graphite oxide structures and obtaining the fibrous mesoporous CNFs proved difficult. High-temperature graphitization at 2800 °C removed the amorphous phase and increased the order of graphitic structure; thus, the CNFs readily developed mesoporous channels oriented along the graphene layers (Supporting Information, Figure S5).

The above-mentioned typical CNFs with platelet, herringbone, and tubular structures were further treated by graphitization and subjected to similar oxidation and heat expansion.

dx.doi.org/10.1021/cm200892c |*Chem. Mater.* 2011, 23, 4141–4148

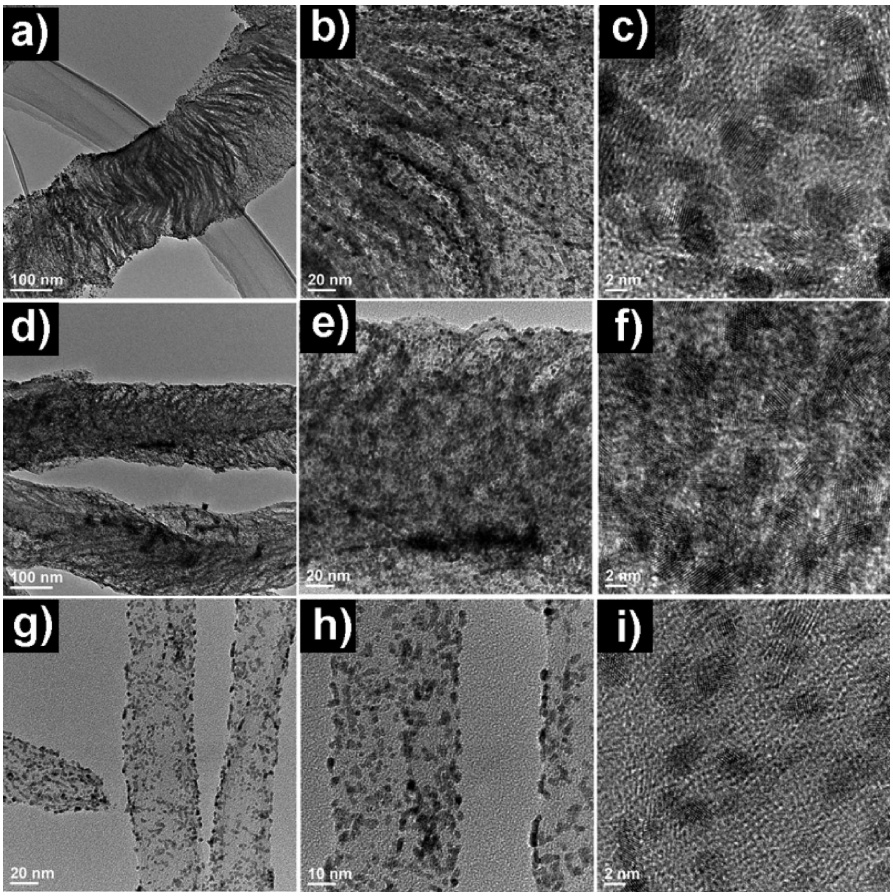

Figure 7. TEM images of MG-CNFs-supported Pt nanoparticles. (a−c) Pt/MG-PCNFs, (d−f) Pt/MG-HCNFs, and (g−i) Pt/MG-TCNFs.

Graphitization caused structural rearrangement and order, as shown in Figure 6 and in the Supporting Information, Figure S6. After oxidation and heat expansion, the mesopores were easily inserted in the graphitized CNFs as a result of the high graphitization degree. The graphitic layers in mesoporous graphitized CNFs became more ordered compared to those in MG-CNFs according to TEM observations. Meanwhile, the mesopore development in the platelet, herringbone, and tubular CNFs became more distinct from those of the MG-CNFs. The BET surface areas of the mesoporous graphitized CNFs were 307, 215, and 148 $m^2\ g^{-1}$ for platelet, herringbone, and tubular structures, respectively, which is smaller than those of MG-CNFs.

Preparation of Pt/MG-CNFs and Their Electrocatalytic Properties. We considered that these highly graphitic structures with large, accessible external surface areas could serve as platinum supports for high-performance fuel cells. In this study, MG-CNF-supported Pt nanoparticles (Pt/MG-CNFs) were prepared using a modified ployol reduction method.[26] The nominal Pt loading was ∼40 wt %. Figure 7 shows the TEM images of the Pt/MG-CNFs with platelet, herringbone, and tubular structures, respectively. Pt nanoparticles were highly dispersed on the external surface of the MG-CNF support. These Pt nanoparticles had very narrow particle size distribution with the average size ∼ 3.2 nm, regardless of the support structure. XRD patterns (Supporting Information, Figure S7) indicated that the Pt nanoparticles had a face-centered cubic structure, and the mean crystallite sizes estimated from the Scherer's formula were consistent with the particle sizes observed in the corresponding TEM images, confirming the presence of single crystals. After 40 wt % Pt loading, the Pt/MG-CNFs catalysts exhibited BET surface areas of 170, 122, and 94 $m^2\ g^{-1}$ for platelet, herringbone, and tubular structures, respectively.

The electrochemically active surface areas (ECSAs) of the Pt/MG-CNFs were determined by H adsorption using cyclic voltammograms (Figure 8a). Characteristic peaks in the negative region were attributed to atomic hydrogen adsorption on the Pt surface. The ECSAs of Pt supported on the platelet, herringbone, and tubular MG-CNFs were calculated to be ∼62, 48, and 89 $m^2\ g^{-1}$ Pt, respectively, which were significantly larger than those of commercial E-TEK XC-72 carbon-supported 40 wt % Pt catalysts (40 $m^2\ g^{-1}$). The uniform distribution of the catalyst and the smaller particle size should be the reason for the enlarging ECSAs.

The electrocatalytic activities of the Pt/GNFs were investigated by voltammetry in a 1.0 M CH_3OH/0.5 M H_2SO_4 solution (Figure 8b). The mass activity (Am) of the catalysts followed the order of Pt/MG-TCNFs (376 mA·mg Pt^{1-}) > Pt/MG-PCNFs (250 mA·mg Pt^{1-}) > Pt/MG-HCNFs (194 mA·mg Pt^{1-}) > Pt/XC-72 (147 mA·mg Pt^{1-}). The Am values corresponded to specific activities (Am/ESA) of 4.2, 4.0, 4.0, and 3.7 A m^{-2}, respectively. Both the Am and the Am/ESA of Pt/MG-CNFs were higher than those of commercial Pt/XC-72 as a result of higher dispersion and higher graphitic support structures. The alignment of the carbon supports for graphene structures was also a key factor affecting the electrocatalytic performance of Pt-carbon catalysts. In this work, the MG-TCNFs supported Pt nanoparticles showed the best electrocatalytic properties, possibly as

dx.doi.org/10.1021/cm200892c |*Chem. Mater.* 2011, 23, 4141–4148

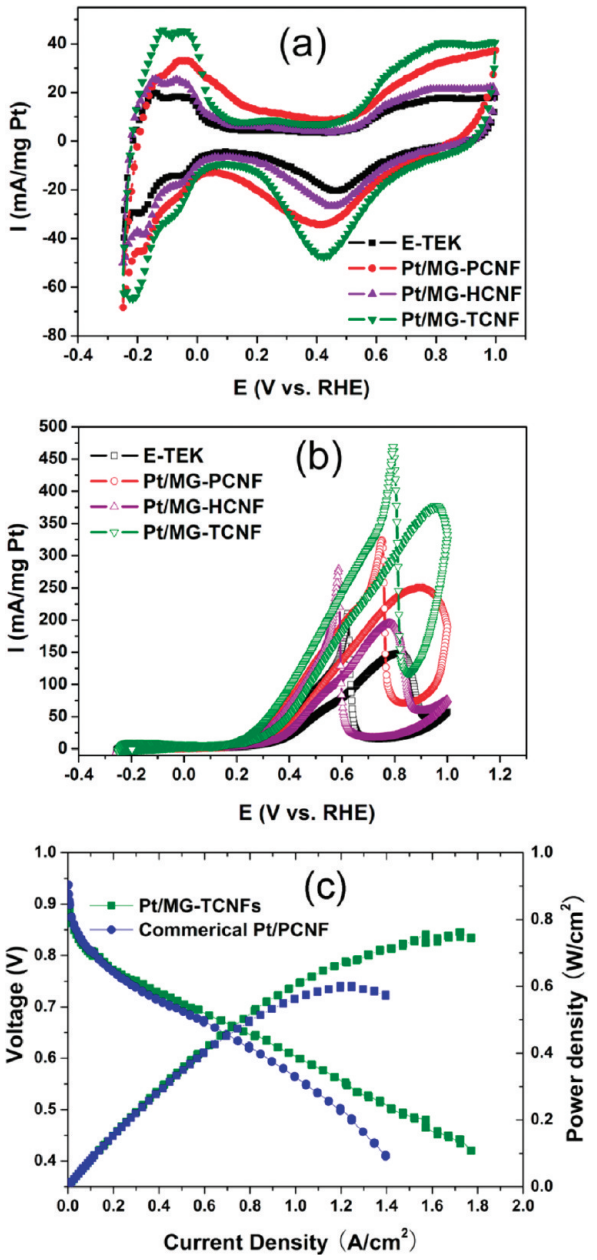

Figure 8. Cyclic voltammograms of the Pt/MG-CNFs catalysts in 0.5 M H_2SO_4 solution saturated by N_2 with a scan rate of 50 mV s^{-1} (a) and in 1.0 M methanol/0.5 M H_2SO_4 solution saturated by N_2 with a scan rate of 20 mV s^{-1} (b). (c) Polarization curves for a direct methanol fuel cell using Pt/MG-TCNFs catalysts and commercial PCNFs supported catalysts.

a result of the high ECSAs and high conductivity of TCNFs, with continuous graphene planes parallel to the axis.

The final requirement for carbon-supported catalysts is their successful application to the electrodes in actual direct methanol fuel cell (DMFC) systems consisting of polymer membranes and electrodes. Figure 8c shows the polarization curves of a DMFC at 70 °C using the Pt/MG-TCNFs as the anode in a single cell system. For comparison, the commercial PCNF supported 40% Pt catalyst from Suntel Co. was also provided, which exhibited very high activity as far as our knowledge. At 0.6 V, an activation polarization regime dominated the activity of the catalyst. The current density of the Pt/MG-TCNFs was 1.02 A cm^{-2}, which was higher than that of the commercial catalyst. In addition, the Pt/MG-TCNFs produced a higher maximum power density, which was 130% higher than that of the commercial catalyst. The excellent performance of the Pt/MG-TCNFs is due mainly to the superior electrocatalytic activity for methanol oxidation of the supported catalyst. Identification of the support properties that were responsible for the enhanced performance requires more comprehensive testing; thus, a more detailed study using MG-CNFs as fuel cell supports is warranted. Detailed studies on the origins of the excellent performance of the MG-CNFs-supported catalysts will be reported in the future.

CONCLUSIONS

In summary, a facile method based on oxidation-heat treatment was developed to insert mesoporous channels into highly graphitic CNFs. The as-prepared MG-CNFs maintained their parent CNF fibrous form and graphene layer alignment, but they developed mesopores with aligned channels. The pore alignment reflected the intrinsic structure of the CNFs, which was controlled by chemical vapor decomposition conditions. The as-prepared mesoporous CNFs exhibited large external surface area and good crystallinity. From the combined results of the electrochemical cell and the practical unit cell, we conclude that as-prepared mesoporous CNFs were excellent supports for the electrodes of direct methanol fuel cells. These materials are also expected to be tailored for applications such as selective adsorption, chromatography, catalytic supports for organic reactions, and electrochemical devices.

ASSOCIATED CONTENT

Supporting Information. Experimental details and supplementary experimental evidence. This material is available free of charge via the Internet at http://pubs.acs.org.

AUTHOR INFORMATION

Corresponding Author

*Tel: +86 21 64252924. Fax: +86 21 64252914. E-mail: longdh@mail.ecust.edu.cn (D.L.).

*Tel: +81 92 583 7959. Fax: +81 92 583 7897. E-mail: yoon@cm.kyushu-u.ac.jp (S.-H.Y.).

REFERENCES

(1) De Jong, K. P.; Geus., J. W. *Catal. Rev.—Sci. Eng.* **2000**, *42*, 481–510.
(2) Yang, P. T.; Chen, J. P. *J. Catal.* **1989**, *115*, 52–64.
(3) Baker, R. T. *Carbon* **1989**, *27*, 315–323.
(4) Guldi, D. M.; Martin, N. *Carbon Nanotube and Related Structures*; Wiley-VCH: Germany, 2010.
(5) Biro, L. P.; Bernardo, C. A.; Tibbetts, G. G.; Lambin, Ph. *Carbon Filaments and Nanotubes: Common Origins, Differing Applications?*; Kluwer Academic Publishers: Dordrecht, Boston, London, 2001.
(6) Rodriguez, N. M. *J. Mater. Res.* **1993**, *8*, 3233–3250.
(7) Rodriguez, N. M.; Chambers, A.; Baker, R. T. K. *Langmuir* **1995**, *11*, 3862–3866.
(8) Bessel, C.; Lanbernds, K.; Rodriquez, N. M.; Baker, R. T. K. *J. Phys. Chem. B* **2001**, *105*, 1115–1118.
(9) Zhang, J.; Hu, Y. S.; Tessonnier, J. P.; Weinberg, G.; Maier, J.; Schlogl, R.; Su, D. S. *Adv. Mater.* **2008**, *20*, 1450–1455.
(10) Dillon, A.; Heben, M. *Appl. Phys. A: Mater. Sci. Process.* **2001**, *72*, 133–142.

(11) Tibbetts, G. G.; Meisner, G. P.; Olk, C. H. *Carbon* **2001**, *39*, 2291–2301.
(12) Hammel, E.; Tang, X.; Trampert, M.; Schmitt, T.; Mauthner, K.; Eder, A.; Pötschke, P. *Carbon* **2004**, *42*, 5–6.
(13) Chinthaginjala, J. K.; Seshan, K.; Lefferts, L. *Ind. Eng. Chem. Res.* **2007**, *46*, 3968–3978.
(14) Taboada, C. D.; Batista, J.; Pintar, A.; Levec, J. *Appl. Catal., B* **2009**, *89*, 375–382.
(15) Serp, P.; Corrias, M.; Kalck, P. *Appl. Catal., A* **2003**, *253*, 337–358.
(16) Lim, S. Y.; Hong, S. H.; Qiao, W. M.; Whitehurst, D. D.; Yoon, S. H.; Mochida, I.; An, B.; Yokogawa, K. *Carbon* **2007**, *45*, 173–179.
(17) Xia, W.; Kundu, S.; Wang, Y. M.; Somsen, C.; Eggeler, G.; Sun, G. H.; Grundmeier, G.; Stratmann, M.; Muhler, M. *Adv. Mater.* **2007**, *19*, 3648–3652.
(18) Yoon, S. H.; Lim, S. Y.; Song, Y.; Ota, Y.; Qiao, W.; Tanaka, A.; Mochida, I. *Carbon* **2004**, *42*, 1723–1729.
(19) Jimenez, V.; Sanchez, P.; de Lucas, A.; Valverde, J. L.; Romero, A. *J. Colloid Interface Sci.* **2009**, *336*, 226–234.
(20) Luxembourg, D.; Py, X.; Didion, A.; Gadiou, R.; Vix-Guterl, C.; Flamant, G. *Microporous Mesoporous Mater.* **2007**, *98*, 123–231.
(21) Gao, W.; Alemany, L. B.; Ci, L.; Ajayan, P. M. New Insights Into the Structure and Reduction of Graphite Oxide *Nat. Chem.* **2009**, *1*, 403–408.Electrochemical Activity of Pt Nanoclusters. *Electrochem. Commun.* **2010**, *12*, 1206−1209.
(22) Yoon, S.; Lim, S.; Hong, S.; Qiao, W.; Whitehurst, D. D.; Mochida, I.; An, B.; Yokogawa, K. *Carbon* **2004**, *43*, 1828–1838.
(23) Tanaka, A.; Yoon, S.; Mochida, I. *Carbon* **2004**, *42*, 591–597.
(24) Hummers, W. S.; Offeman, R. E. *J. Am. Chem. Soc.* **1958**, *80*, 1339.
(25) Yang, S. Y.; Chang, K. H.; Lee, Y. F.; Ma, C. C. M.; Hu, C. C. *Electrochem. Commun.* **2010**, *12*, 1206.
(26) He, H.; Riedl, T.; Lerf, A.; Klinowski, J. *J. Phys. Chem.* **1996**, *100*, 19954–19958.
(27) Lerf, A.; He, H.; Forster, M.; Klinowski, J. *J. Phys. Chem. B* **1998**, *102*, 4477–4482.
(28) He, H.; Klinowski, J.; Forster, M.; Lerf, A. *Chem. Phys. Lett.* **1998**, *287*, 53–56.